

REPORT DOCUMENTATION PAGE				Form Approved OMB No. 0704-0188	
Public reporting burden for this collection of information is estimated to average 1 hour per response, including the time for reviewing instructions, searching existing data sources, gathering and maintaining the data needed, and completing and reviewing this collection of information. Send comments regarding this burden estimate or any other aspect of this collection of information, including suggestions for reducing this burden to Department of Defense, Washington Headquarters Services, Directorate for Information Operations and Reports (0704-0188), 1215 Jefferson Davis Highway, Suite 1204, Arlington, VA 22202-4302. Respondents should be aware that notwithstanding any other provision of law, no person shall be subject to any penalty for failing to comply with a collection of information if it does not display a currently valid OMB control number. PLEASE DO NOT RETURN YOUR FORM TO THE ABOVE ADDRESS.					
1. REPORT DATE (DD-MM-YYYY) 10-08-2011		2. REPORT TYPE Conference Paper		3. DATES COVERED (From - To)	
4. TITLE AND SUBTITLE Demonstration of Laser-Induced Fluorescence on Krypton Hall Effect Thruster				5a. CONTRACT NUMBER	
				5b. GRANT NUMBER	
				5c. PROGRAM ELEMENT NUMBER	
6. AUTHOR(S) William A. Hargus Jr., Gregory X. Azarnia, and Michael R. Nakles				5d. PROJECT NUMBER	
				5f. WORK UNIT NUMBER 33SP0706	
7. PERFORMING ORGANIZATION NAME(S) AND ADDRESS(ES) Air Force Research Laboratory (AFMC) AFRL/RZSS 1 Ara Road Edwards AFB CA 93524-7013				8. PERFORMING ORGANIZATION REPORT NUMBER AFRL-RZ-ED-TP-2011-345	
9. SPONSORING / MONITORING AGENCY NAME(S) AND ADDRESS(ES) Air Force Research Laboratory (AFMC) AFRL/RZS 5 Pollux Drive Edwards AFB CA 93524-7048				10. SPONSOR/MONITOR'S ACRONYM(S)	
				11. SPONSOR/MONITOR'S NUMBER(S) AFRL-RZ-ED- TP-2011-345	
12. DISTRIBUTION / AVAILABILITY STATEMENT Approved for public release; distribution unlimited (PA #11605).					
13. SUPPLEMENTARY NOTES For presentation at the 32 nd International Electric Propulsion Conference, Wiesbaden, Germany, 11-15 Sep 2011.					
14. ABSTRACT There is growing interest within the electrostatic propulsion community for the use of krypton as a propellant. It is a lower cost replacement for xenon, and is especially of interest for potentially very large solar electric transfer vehicles that may potentially strain xenon production capability. Understanding the subtleties of changing the propellant requires the development of new diagnostic capabilities that can probe thruster krypton propellant acceleration with the minimum disturbance to the overall propellant stream similar to those already developed for xenon. This study presents the application of laser- induced fluorescence as a plasma diagnostic technique for singly ionized krypton. Using the 728.98 nm $5d^4D_{7/2}-5p^4P^{\circ}_{5/2}$ Kr II transition, we successfully measured ion velocities in the near-plume and within the acceleration channel of a laboratory model, low power Hall effect thruster. A preliminary comparison to previous xenon ion laser-induced fluorescence measurements of the same thruster indicate substantially narrowed fluorescence lineshapes, presumed to be due to decreases in plasma turbulence of the krypton operation compared to xenon. However, overall propellant energy deposition and effective electric fields calculated from the bulk ion velocities were remarkably similar.					
15. SUBJECT TERMS					
16. SECURITY CLASSIFICATION OF:			17. LIMITATION OF ABSTRACT	18. NUMBER OF PAGES	19a. NAME OF RESPONSIBLE PERSON
a. REPORT	b. ABSTRACT	c. THIS PAGE			Dr. William A. Hargus, Jr.
Unclassified	Unclassified	Unclassified	SAR	13	19b. TELEPHONE NUMBER (include area code) N/A

Demonstration of Laser-Induced Fluorescence on a Krypton Hall Effect Thruster

William A. Hargus, Jr.*

Gregory M. Azarnia†

Michael R. Nakles‡

Air Force Research Laboratory, Edwards Air Force Base, CA 93524

There is growing interest within the electrostatic propulsion community for the use of krypton as a propellant. It is a lower cost replacement for xenon, and is especially of interest for potentially very large solar electric transfer vehicles that may potentially strain xenon production capability. Understanding the subtleties of changing the propellant requires the development of new diagnostic capabilities that can probe thruster krypton propellant acceleration with the minimum disturbance to the overall propellant stream similar to those already developed for xenon. This study presents the application of laser-induced fluorescence as a plasma diagnostic technique for singly ionized krypton. Using the 728.98 nm $5d^4D_{7/2}-5p^4P_{5/2}^o$ Kr II transition, we successfully measured ion velocities in the near-plume and within the acceleration channel of a laboratory model, low power Hall effect thruster. A preliminary comparison to previous xenon ion laser-induced fluorescence measurements of the same thruster indicate substantially narrowed fluorescence lineshapes, presumed to be due to decreases in plasma turbulence of the krypton operation compared to xenon. However, overall propellant energy deposition and effective electric fields calculated from the bulk ion velocities were remarkably similar.

Introduction

At present, xenon (Xe) is the propellant of choice for most electrostatic plasma thrusters including Hall effect thrusters. The selection of xenon is due to a number of rigorous engineering rationale. These include the high mass (131 amu) and relatively low ionization potential (12.1 eV) of xenon; as well as the inert nature of xenon, which eliminates much of the controversy that plagued early electrostatic propulsion efforts when mercury (Hg) and cesium (Cs) were the propellants of choice.¹ Although xenon is a noble gas, it is the heaviest, and due to its non-ideal gas behavior, it is possible to pressurize and store with room temperature specific densities approaching 1.6.^{2,3} As such, it may be stored at higher densities than that of the most common liquid monopropellant, hydrazine, which as a specific gravity of approximately 1.

While xenon may remain an ideal propellant for electrostatic thrusters such as Hall effect thrusters, there are several concerns that have driven the Hall effect thruster community to explore alternative propellants. As orbit raising missions of longer duration and larger payloads are proposed, requisite propellant mass increases dramatically. Xenon production is a byproduct of the fractional distillation of atmospheric gases for use primarily by the steel industry. Due to the low concentration of xenon in the atmosphere (~ 90 ppb), worldwide production is only

approximately 6,000 standard cubic meters per year. Increasing industrial demand for items such as high efficiency lighting and windows, as well as plasma based micro-fabrication, has produced wide price swings in the past decade. Xenon prices have varied by as much as factor of ten in the past four years alone.

For missions that can benefit from higher specific impulse, krypton may have benefits beyond its lower cost. Krypton has a lower atomic mass (83.8 amu), but a slightly higher ionization potential (14.0 eV) than xenon. Like xenon, krypton is a noble gas and could be easily integrated into existing Hall effect thruster propellant management systems without much modification. The similar ionization potential should not dramatically affect Hall effect thruster efficiency, and the lower atomic mass could produce a 25% increase in specific impulse. The increase in specific impulse may be useful for missions such as station-keeping where increased specific impulse is advantageous. For missions such as orbit raising, increasing the specific impulse may increase trip time due to power limitations. However as solar electric power system specific power decreases, increasing the specific impulse of the propulsion system can maintain trip time while reducing total system mass. Krypton is approximately $10\times$ more common in the atmosphere (and hence in production) than xenon, and when accounting for mass is approximately $6\times$ less expensive. Table 1 summarizes the properties of xenon and krypton.²

In order to assess whether the potential advantages

*Senior Engineer, AFRL/RZSS, Edwards AFB, CA, USA.

†Scientist, ERC, Inc., Edwards AFB, CA, USA

‡Senior Engineer, ERC, Inc., Edwards AFB, CA, USA

Table 1 Comparison of xenon and krypton properties critical for electrostatic propulsion.²

Property	Units	Xe	Kr
Atomic Mass	amu	131.3	83.8
1 st Ionization Energy	eV	12.1	14.0
2 nd Ionization Energy	eV	21	24
3 rd Ionization Energy	eV	32	37
Atmospheric Concentration	ppb	87	1000
Stable Isotopes		9	6
Odd Isotopes		2	1
Critical Pressure	MPa	5.84	5.50
Critical Temperature	K	290	209
Boiling Point (1 atm)	K	161	120

of krypton propellant can be realized in Hall effect thrusters and other electrostatic thruster types, experimental measurements of these plasmas must be obtained, both to determine relative figures of functional merit and for numerical simulation validation for increased fundamental understanding of subtle propellant effects. Many diagnostics previously developed for xenon plasmas can be applied with little modification. These include critical performance measures (e.g. thrust measurements using inverted pendulum thrust stands) and most electrostatic probes for far-plume characterization (e.g. Faraday probes for ion flux measurements, retarding potential analyzers for ion energy distributions, etc.). However, optical measurements such as laser-induced fluorescence, which can provide spatially resolved velocity distribution measurements, are species dependent and require significant retooling when applied to new propellants. This work examines theoretical development and first time application of laser-induced fluorescence of a krypton ion transition both within the acceleration channel and near-plume of a plasma thruster.

Laser-Induced Fluorescence

Laser-induced fluorescence (LIF) may be used to detect velocity-induced shifts in the spectral absorption of various plasma species. The fluorescence is monitored as a continuous-wave laser is tuned in frequency over the transition of interest, of energy $h\nu_{12}$, where h is Plank's constant, ν_{12} is wavenumber of transition between lower state 1 and higher energy state 2. Note that state 1 may be the ground state, but any sufficiently highly populated excited state will do. In this work, we have chosen to examine a metastable state to ensure highest signal levels. Measurements can be made with high spatial resolution, determined by the intersection of the probe laser beam with the fluorescence optical collection volume.

Velocity measurements may be made using LIF velocimetry as an atom, or as in our case an ion, moving with a velocity component u relative to the direction of

the incoming laser will absorb photons at a frequency shifted from that of stationary absorbers due to the Doppler effect. The magnitude of this frequency shift $\delta\nu_{12}$ is

$$\delta\nu_{12} = \frac{u}{c}\nu_{12}. \quad (1)$$

The measured fluorescence lineshape is determined by the environment of the absorbing ion population, so an accurate measurement of the lineshape function may lead to the determination of a number of plasma parameters beyond simple bulk velocities. The precision of measured velocities has been found, in various studies, to be less than the experimental uncertainty for the ions (± 500 m/s).⁴⁻⁶

LIF is a convenient diagnostic for the investigation of ion velocities in a plasma thruster as it does not physically perturb the discharge. The LIF signal is a convolution of the velocity distribution function (VDF), transition lineshape, and laser beam frequency profile. Determination of the VDF from LIF data only requires the deconvolution of the transition lineshape and laser beam profile from the raw LIF signal trace. Alternatively, the lineshape itself may also provide valuable information on the state of the plasma, such as electron density, pressure, or heavy species temperature. In the somewhat turbulent plasmas typical of Hall effect thrusters, the fluorescence lineshape can also be indicative of the relative motion of the ionization zone as it axially traverses in the periodic breathing mode plasma fluctuation.^{7,8} However, care must be taken to ensure that the relative effects of these phenomena are separable. In addition, magnetic (Zeeman effect) and electric (Stark effect) fields may also influence the fluorescence lineshape⁹ and must be accounted for when analyzing the lineshapes should the fields be of sufficient magnitude. In the case of LIF of ions in a Hall effect thruster, the fluorescence lineshape appears to be most indicative of the aforementioned plasma turbulence including periodicity in the positions of the ionization zone within the acceleration channel.

Krypton Ion Spectroscopy

Hyperfine Effects

Of the 31 known isotopes of Kr, only six have atmospheric concentrations greater than 0.3%. Of these six isotopes between 78 amu and 86 amu, only one, ⁸³Kr has an odd number of neutrons (recall that krypton's atomic number is 36).² This is important in the high resolution analysis of atomic spectra since each will have a slight difference in their electron transition energies due to their differences in nuclear mass. This effect has been described in detail previously for xenon in the development of Hall thruster laser diagnostics^{4,10}

The odd mass isotopes are further spin split due to nuclear magnetic dipole and electric quadrupole

Table 2 Naturally Occurring Krypton Isotope Properties.^{2,11}

Mass (amu)	Abundance	Nuclear Spin
78	0.35%	0
80	2.27%	0
82	11.56%	0
83	11.55%	$\frac{9}{2}$
84	56.90%	0
86	17.37%	0

moments. Nuclei which have an odd number of protons and/or an odd number of neutrons possess an intrinsic nuclear spin $\mathbf{I}\hbar/2\pi$, where \mathbf{I} is integral or half-integral depending on if the atomic mass is even or odd, respectively¹² and boldface is used to denote vector quantities. For nuclei with non-zero nuclear spin (angular momentum, \mathbf{J}), the interaction of the nucleus with the bound electrons lead to the splitting of levels with \mathbf{J} into a number of components, each corresponding to a specific value of the total angular momentum $\mathbf{F} = \mathbf{I} + \mathbf{J}$.¹³ As a result of this interaction, \mathbf{F} is a conserved quantity while \mathbf{I} and \mathbf{J} individually are not. The interaction is weak, allowing the hyperfine splitting of each level to be taken independently of the other levels. The number of nuclear spin split hyperfine components is $2I + 1$ if $J \geq 1$ and $2J + 1$ if $J < 1$, with F taking on the values $F = J + I, J + I - 1, \dots, |J - I|$ while satisfying the selection rules imposed on F , i.e. $\Delta F = 0, \pm 1$, unless $F = 0$, in which case $\Delta F \neq 0$.

With these selection rules on the quantum numbers for a particular electronic transition, and with knowledge of the hyperfine structure constants which characterize the magnetic dipole and electric quadrupole moments of the nucleus,¹² the hyperfine energy shifts from the position of the energy for the unshifted level with angular momentum J can be easily calculated.^{10,14} The relative intensities of transitions between these levels are derived assuming Russel-Saunders coupling,¹⁴ allowing the complete construction of the fluorescence lineshape. Of course, the intensities of the isotope shifted transitions are proportional to each isotopes relative abundance.

Two constants are associated with the magnitude of hyperfine nuclear spin splitting.¹² These are the A hyperfine structure constant which represents the nuclear magnetic dipole effect on the atom, and the B hyperfine structure constant which is associated with the nuclear electric quadrupole moment of the atom which will only be present if $I \geq 1$. The relative energy of the spin split states depends on the sign of A . In atoms with $A > 0$, the state with the highest value of F has the highest energy. While for atoms with $A < 0$, the state with the lowest value of F has the highest energy.¹⁴ The energy level shift ΔE_M associated with the magnetic dipole of the nucleus is given by Cowan.¹²

$$\Delta E_M(F) = \frac{1}{2}A[F(F+1)J(J+1)I(I+1)] = \frac{A}{2}C \quad (2)$$

Additionally, the energy spacing between successive levels $F - 1$ and F may be shown to be proportional to F .

$$\Delta E_M(F) - \Delta E_M(F - 1) = AF \quad (3)$$

If $I \geq 1$, the nucleus will have an electric quadrupole moment and a related hyperfine splitting constant B which produces an additional hyperfine splitting with energy linear in $C(C+1)$ where C is previously defined in Eqn. 2.

$$\Delta E_F = \Delta E_M + \Delta E_Q \quad (4)$$

$$\Delta E_F = \frac{AC}{2} + \frac{B[\frac{3}{2}C(C+1)2I(I+1)J(J+1)]}{4I(2I-1)J(2J-1)} \quad (5)$$

Where ΔE_F is the combined nuclear spin split energy level shift combining the effect from the nuclear magnetic dipole moment ΔE_M and the effect of the electric quadrupole moment ΔE_Q .¹² It should be noted that the center of gravity of the hyperfine levels lies at a position of the unsplit level J .¹³

$$\sum_F (2F+1)\Delta E_F \quad (6)$$

Due to close energy spacing of nuclear spin split levels, near ideal coupling between \mathbf{I} and \mathbf{J} occurs in most hyperfine structure. Therefore, the intensity S rules derived by White for Russel-Saunders coupling are appropriate for hyperfine splitting.¹⁴

For $J - 1 \rightarrow J$,

$F - 1 \rightarrow F$:

$$S = \kappa \frac{(Q+I+1)(Q+I)(Q-I)(Q-I-1)}{F} \quad (7)$$

$F \rightarrow F$:

$$S = -\kappa \frac{(Q+I+1)(Q-I)(W+I)(W-I-1)(2F+1)}{F(F+1)} \quad (8)$$

$F + 1 \rightarrow F$:

$$S = \kappa \frac{(W+I)(W+I-1)(W-I-1)(W-I-2)}{F+1} \quad (9)$$

For $J \rightarrow J$,

$F - 1 \rightarrow F$:

$$S = -\kappa \frac{(Q + I + 1)(Q - I)(W + I + 1)(W - I)}{F} \quad (10)$$

$F \rightarrow F$:

$$S = \kappa \frac{[J(J + 1) + F(F + 1) + I(I + 1)]^2(2F + 1)}{F(F + 1)} \quad (11)$$

$F + 1 \rightarrow F$:

$$S = -\kappa \frac{(Q + I + 2)(Q - I + 1)(W + I)(W - I - 1)}{(F + 1)} \quad (12)$$

Where S is the transition strength and κ is an arbitrary constant. The variables $Q = J + F$ and $W = J - F$ are only introduced to compress the notation.

The relative intensities of the isotope shifted transitions are proportional to each isotope's relative abundance. However, the relative intensities of the nuclear spin split hyperfine splitting are governed by two summation rules.¹³ First, the sum of the intensities of all the lines of the hyperfine structure of a transition $J \rightarrow J'$ originating from a component F of the level J is proportional to the statistical weight of this component, $(2F + 1)$. Second, the sum of the intensities of all the lines of the hyperfine structure the transition $J \rightarrow J'$ ending on the component F' of the level J' is proportional to the statistical weight of this component, $(2F' + 1)$. With these two sum rules, a system of linear equations are solved for the relative intensities of the nuclear spin split components of each isotope.

The practical issues associated with hyperfine isotopic spin splitting in the measurements of plasma acceleration in the plume and within Hall effect thrusters are that the even isotopes broaden the line width to some degree, while the odd isotopes may create much more complex transition structure in high resolution. To some extent, hyperfine spin splitting can be neglected for some transitions. For example, the $5d[4]_{7/2} - 6p[3]_{5/2}$ spin split electronic transition of Xe II at 834.72 nm is relatively narrow at approximately 500 MHz and the line structure can be neglected to a large degree in analysis of Hall effect thruster plasma dynamics.^{15,16} However, the Xe I $6s[3/2]_2^0 - 6p[3/2]_2$ transition at 823.18 nm is dramatically broader and visually more complex due to the spin split odd isotopes.¹⁰ Furthermore as the mass of the atoms of interest is lowered, the energy separation between the various isotope's transitions increases as the fractional changes in nuclear mass increase. As a

Table 3 Spin Splitting Constants for the $^{83}\text{Kr II } 5d^4D_{7/2} - 5p^4P_{5/2}^\circ$ transition at 728.98 nm^{18,19}

Electronic State	A Coefficient MHz	B Coefficient MHz
$5d^4D_{7/2}$	-43.513	-294.921
$5p^4P_{5/2}^\circ$	-167.2	+91

Table 4 Isotope Shifts for the Kr II $5d^4D_{7/2} - 5p^4P_{5/2}^\circ$ transition at 728.98 nm¹⁹

Isotope	Isotope Shift MHz
78	1185.7
80	768.0
82	372.6
83	175.0
84	0
86	-365.2

result, knowledge of these isotope constants becomes increasingly important to adequately interpret the fluorescence spectra.

Kr II Transition at 728.98 nm

The most recent review of Kr II transitions suitable for diagnostics of plasma thrusters is by Scharfe.¹⁷ His survey of available transitions has identified only a single transition where both the isotope and spin split hyperfine constants are known. The Kr II $5d^4D_{7/2} - 5p^4P_{5/2}^\circ$ transition at 728.98 nm has received the most study of the several lines identified by Scharfe.

Scholl, et al.¹⁸ measured the lower $5d^4D_{7/2}$ state A and B spin splitting constants for ^{83}Kr to high accuracy as shown in Table 3. While Schuessler et al.¹⁹ measured the spin splitting constants for the upper $5p^4P_{5/2}^\circ$ state also shown in Table 3. Schuessler et al. also measured the isotope shifts of the 728.98 nm $5d^4D_{7/2} - 5p^4P_{5/2}^\circ$ transition as shown in Table 4. From our research as well as that performed by Scharfe, it appears that this is the only Kr II transition for which the hyperfine structure has been fully characterized.

From the $5p^4P_{5/2}^\circ$ state, there are 6 known transitions for the fluorescence decay. Using available Einstein coefficients for spontaneous emission, there appears to be a transition, $5s^4P_{5/2} - 5p^4P_{5/2}^\circ$, at 473.90 nm with a greater than 80% branching ratio.²⁰ The resonant fluorescence for the $5d^4D_{7/2} - 5p^4P_{5/2}^\circ$ transition appears to be approximately 10%.

Using the information in Tables 3 and 4, the line structure of the 728.98 nm $5d^4D_{7/2} - 5p^4P_{5/2}^\circ$ transition may be modeled. Again, we assume Doppler broadening to be the only significant mechanism in this preliminary analysis.

Figure 1 shows the cold (1 K) transition. As in

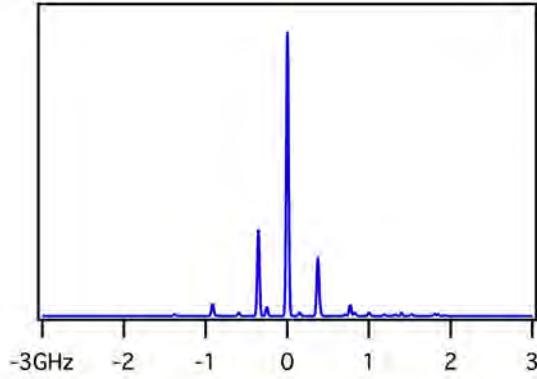


Fig. 1 Cold spectrum (1 K) of the Kr II 728.98 nm $5d^4D_{7/2}-5p^4P_{5/2}^o$ transition.

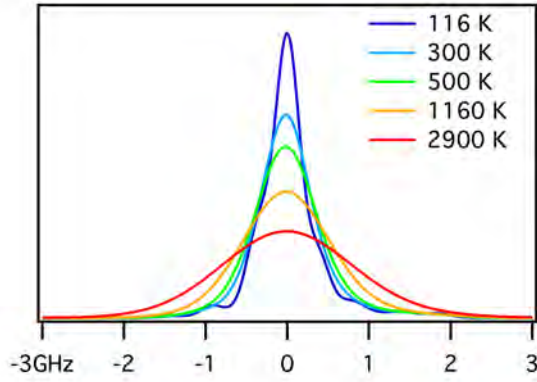


Fig. 2 Multitemperature spectrum of the Kr II 728.98 nm $5d^4D_{7/2}-5p^4P_{5/2}^o$ transition.

the case of the neutral transition, the higher peaks represent the even isotopes while the more outlying, lower magnitude peaks are due to the spin split ^{83}Kr isotope.

Figure 2 shows the lineshape for a variety of temperatures, up to 2900 K, or 0.25 eV. Temperatures above 0.25 eV do not exhibit any visible structure. This upper limit was chosen based on previous measurements which showed that the ion temperatures, as near as they can be defined, are low as measured in radial measurements.⁴ In fact, the lineshape in the axial direction actually appears to be dominated by discharge plasma dynamics and these are reflected in the axial fluorescence lineshape.¹⁶

It is interesting to note that the isotope shifts are significant, and as a result, Fig. 2 shows a clear broadening of the line cumulative width relative to a single component Doppler width due to the isotope shifts. The difference appears to be a consistent 200 MHz, and it appears to be nearly constant in the range of temperatures examined.

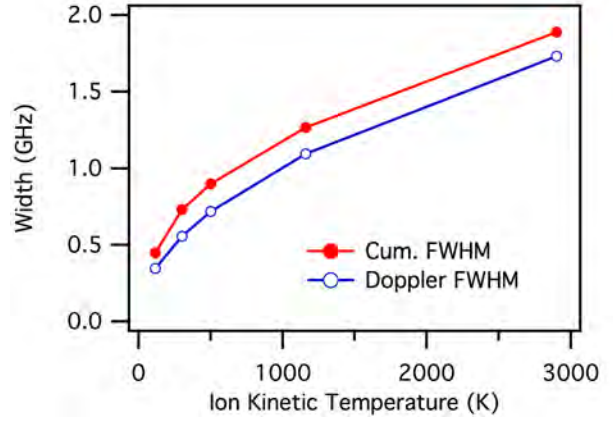


Fig. 3 Cumulative line width (FWHM) and Doppler linewidth compared for the Kr II 728.98 nm $5d^4D_{7/2}-5p^4P_{5/2}^o$ transition.

Apparatus

Vacuum Facility and Thruster

The LIF measurements were performed in Chamber 6 of the Air Force Research Laboratory (AFRL) Electric Propulsion Laboratory at Edwards AFB, CA. Chamber 6 is a non-magnetic stainless steel chamber with a 1.8 m diameter and 3 m length. Pumping is provided by four single stage cryogenic panels (single stage cold heads at 25 K) and one 50 cm two stage cryogenic pump (12 K). This vacuum test chamber has a measured maximum pumping speed of 36,000 L/s on xenon. For this set of tests, two of the cold heads were not operational and the pumping speed is believed to be approximately 18,000 L/s on krypton.

The Hall thruster used in this study is a low power laboratory Hall effect thruster which has been described elsewhere.⁵ This thruster is designed for operation on xenon and performance is not characterized for krypton. Thruster operation for this effort consisted of a single stable condition shown on Table 5. Compared to operation on xenon, krypton operation was unstable at higher magnetic field strengths and lower propellant flow rates. In order to match anode discharge potential to previous xenon measurements (250 V), the flow rate was increased by 24% and the current to the magnetic field was reduced to approximately half of xenon nominal. For the purposes of diagnostics development, the condition chosen for study also consisted of the lowest discharge current oscillation case as determined by fixing the propellant flow rate and varying the magnetic field. At this condition, the total anode current was only increased 15% by this combination likely indicating lower ionization efficiency.

Chamber pressure during thruster operation was measured with a cold cathode ionization gauge and is approximately 1×10^{-3} Pa, corrected for krypton (using an N_2 conversion to Kr multiplicative factor

Table 5 *Nominal thruster operating conditions.*

Kr Anode Flow	10.5 sccm
Kr Cathode Flow	1.0 sccm
Anode Potential	250 V
Anode Current	0.92 A
Keeper Current	0.5 A
Magnet Current	410 mA
Heater Current	3.0 A

of 0.59²¹). During thruster operation, the thruster parameters shown in Table 5 are monitored and recorded at a 0.2 Hz data rate.

Laser and Optics

Upon selection of the Kr II $5d^4D_{7/2}-5p^4P_{5/2}^o$ transition at 728.98 nm ($\Delta E = 13,713.989 \text{ cm}^{-1}$) for further examination, we purchased and took delivery of a custom built ± 50 GHz tunable diode laser (Newport Optics, New Focus Division) centered on the $5d^4D_{7/2}-5p^4P_{5/2}^o$ transition with a maximum of 25 mW output power. This laser is a Littman-Metcalf external cavity tunable diode laser capable of mode hop free tuning across approximately 100 GHz tuning range at output powers as high as 25 mW with a line width of less than 500 kHz.

Based on previous efforts,²² the laser, probe beam launch optics, and fluorescence collection optics are located on two optical tables placed about viewports with optical access into the vacuum chamber as shown in Fig. 4. On the primary optics table, the diode laser beam first passes through a Faraday isolator to eliminate laser feedback. The laser beam then passes through a 10% wedged beam pick-off (PO) to provide beam diagnostics. The first of the two reflections (each approximately 5% of incident power) is directed onto a photodiode detector (D1) and provides constant power feedback to the laser. The second pick-off beam passes through a 300 MHz free spectral range, high finesse Fabry-Perot etalon (F-P) that provides frequency monitoring of the wavelength interval swept during a laser scan.

The main laser beam is then chopped at 3 kHz by a mechanical optical chopper for phase sensitive detection. It is then divided into two equal components by a 50:50 cube beam splitter (BS). The first component passes through a krypton opto-galvanic cell and is terminated by a beam dump. The opto-galvanic cell current is capacitively coupled to a lock-in amplifier in order to monitor the Kr II 728.98 nm $5d^4D_{7/2}-5p^4P_{5/2}^o$ transition to provide a zero velocity reference.²³

The probe beam is then directed via several mirrors and focused by a single lens to a sub-millimeter beam waist within the chamber vacuum through a glass vacuum viewport. The fluorescence collection optics also shown in Fig. 4 collect the signal generated at the beam waist. The fluorescence is collected by a

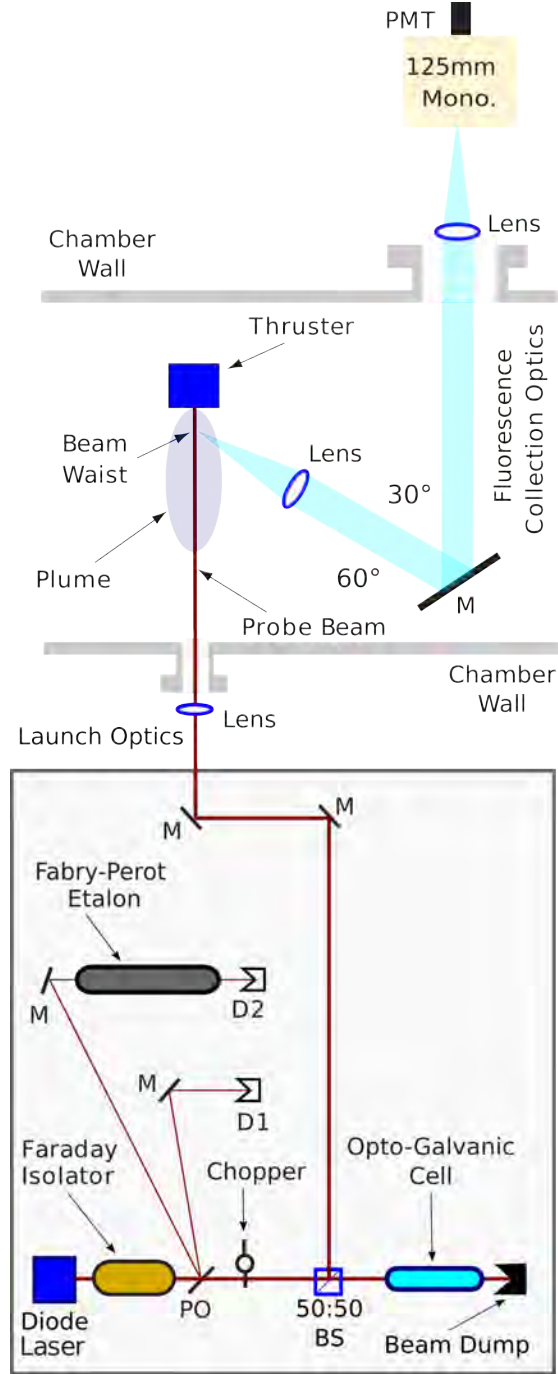


Fig. 4 Layout of Kr II laser-induced fluorescence apparatus showing all relevant optical components, portions of the vacuum chamber, and Hall effect thruster thruster plume.

75 mm diameter, 300 mm focal length lens within the chamber. The collimated signal is directed through a window in the chamber side wall to a similar lens that focuses the collected fluorescence onto the entrance slit of 125 mm focal length monochromator with a photo-multiplier tube (PMT) detector. The PMT signal is then analyzed using a second lock-in amplifier. The spatial resolution of the measurements is determined

Measurements

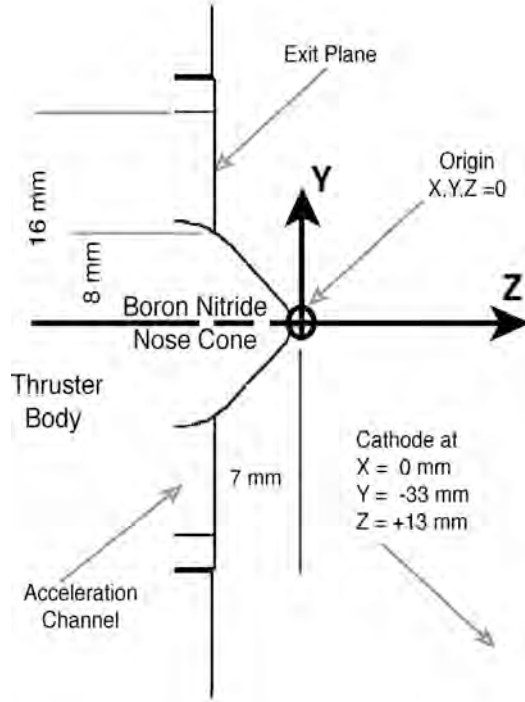


Fig. 5 Near-field dimensions of the low power laboratory Hall effect thruster with origin of the coordinate system and positions of critical dimensions and locations identified.

by the geometry of the spectrometer entrance slit (note the 1:1 magnification of the collection optics).

Measurement Geometry

Within the vacuum chamber, the thruster is mounted on a three axis orthogonal computer controlled translation system, so that the sample volume position may be shifted relative to the fluorescence collection volume defined by the intersection of the probe beam waist and the collection optics focus. Figure 5 shows the near-field geometry of the low power Hall effect thruster examined in this work.²² The locations of the protruding central magnetic pole (nose cone) and geometry of the acceleration channel are indicated as is the position of the cathode exit. The cartesian coordinate system and origin used in these measurements is also shown. The coordinate system origin is 0.5 mm beyond the tip of the nose cone due to the repeatability with which this position may be located. All locations are referenced to these Cartesian coordinates with the indicated origin.

Measurements in this work are limited to the $Z - Y$ plane shown in Fig. 5. Two sets of measurements are presented. The first measurement set is a radial survey of the axial ion velocities at the cathode plane ($Z = +13$ mm) varying radially from near the cathode ($Y = -30$ mm) to a congruent distance in the positive axis ($Y = +40$ mm). This plume measurement set, 20 mm from the exit plane, provides insight into the near-field plume evolution.

The second measurement set is along $Y = +12$ mm, which corresponds to the center of the upper acceleration channel. These axial velocity measurements are between $Z = 0$, the extent of the protruding central pole nose cone; and $Z = -13$ mm, the furthest into the thruster that is optically accessible with the collection optics shown in Fig. 4. This set of measurements characterizes the acceleration within the thruster into the near-plume region.

Determining how to present the experimental results of LIF velocity measurements such as these can be problematic. Since LIF measurements are noise limited, they are often times better suited to determining the *most probable velocity*. This is defined as the peak of the velocity distribution, easily determined by the peak of the fluorescence trace. However in the skewed, non-symmetric velocity distributions common to Hall thrusters, the most probable (i.e. peak signal) and statistical mean velocities often differ. Furthermore, multiple peaks in the fluorescence distribution will occur as various populations overlap with limited interaction in the rarified plasma plume. We will therefore present both analysis; peaks of the distribution due to their singular values, and fluorescence traces for their close approximation to the velocity distributions. No effort shall be made to deconvolve the estimated lineshape from these measurements to more closely determine the velocity distribution at this time.¹⁶ Both representations of these data can provide important insights as to the behavior of the plasma acceleration processes.

Cathode Plane Radial Cross-Section

Figure 6 shows the collected fluorescence at $Y = 0$, $Z = -13$ mm. At this location, we see very good signal to noise ratios (SNR) and a distinct peak shifted approximately 33 GHz from the stationary reference. This shift corresponds to an axial velocity of 17,800 m/s. Also interesting is a small peak with a much smaller magnitude corresponding to a velocity of approximately 500 m/s. Multiple peaks are not unique to this position and have been seen in LIF measurements in prior efforts.^{5,15} It is also difficult to ascribe a singular velocity, or even several velocities, to a measurement. Rather, it is necessary, even in a simple lineshape like that shown in Fig. 6, to consider a continuous distribution of velocities.¹⁶

Accepting that the (sometimes multiple) peaks from

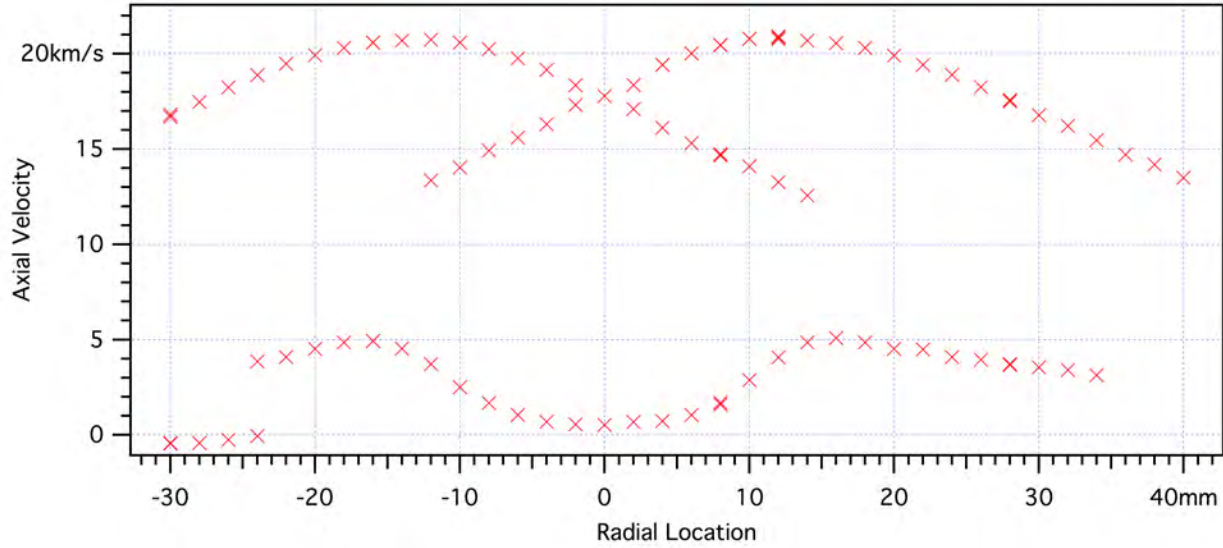


Fig. 7 Axial most probable velocities of all distinguishable peaks in each fluorescence trace at $Y = 13$ mm (20 mm into plume from the exit plane at the geometrical cathode plane).

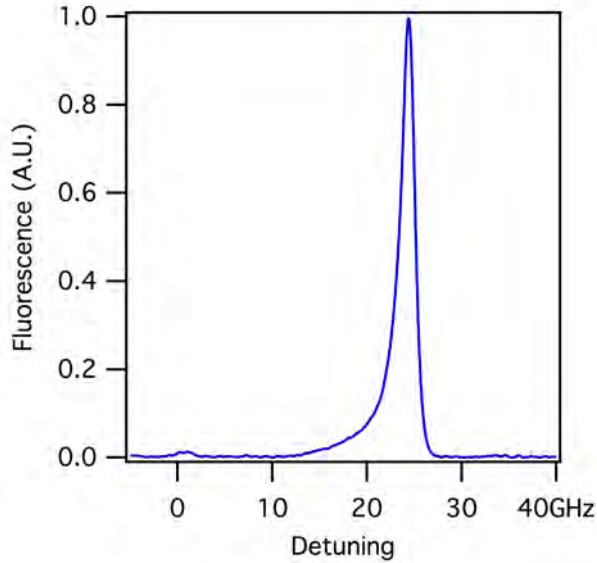


Fig. 6 Laser-induced fluorescence collected at $Y = 13$ mm, $Z = 0$ mm. Note the very small peak near 0 GHz and the main peak at 33 GHz detuning from stationary line center.

the fluorescence distributions represent appropriate assessments of the most probable velocities, we can find the most probable velocities from peaks in the fluorescence traces. Figure 7 shows the velocities calculated from the identifiable peaks in all the LIF traces in the cathode plane radial cross-section measurement set. As seen in Fig. 7, the plume structure evolves as one departs from the $Y = 0$, $Z = -13$ mm trace shown in Fig. 6.

It is immediately evident that the influence of the annular structure of the Hall effect thruster is visible in the velocities identified in the plume in Fig. 7. This is most obvious in the distinct apparent expansion of two

plumes in the highest velocities from opposite sides of the annular acceleration channel. The peak velocities closely correspond to $Y = \pm 12$ mm geometric center of the annular acceleration channel.

In addition to the peak velocity previously discussed, there is a low velocity component in Fig. 7. This low velocity component varies from approximately 500 m/s on centerline to a peak of 5 km/s at $Y = \pm 15$ mm, decreasing slightly at larger radii. We believe that this feature represents a population of late ionized and moderately accelerated ions. The low velocities of this population near the centerline are likely due to the protruding nose cone physically impeding ion flux as well as the requisite annular geometry of the Hall effect thruster. The abrupt change in the velocities at $Y = -24$ mm is due to the cathode ejecting a population of low energy ions nearby. The slight negative velocities (ranging from -200 to -400 m/s) in this region may be due to the cathode plume orientation and the visible plume emanating from the cathode orifice that visually appears to curve toward the anode.

As in Fig. 6, the relative magnitudes of the various peaks can vary significantly. Figure 8 shows how the lineshape with its multiple peaks evolves, starting on the plume centerline and moving outward. On centerline, the highest velocity peak dominates and the slow peak is only evident upon very close examination as in Fig. 6. The highest velocity peak dominates all the subsequent measurements away from the plume centerline with an peak velocity that reaches its maximum at the geometric center of the annular acceleration channel at $Y = \pm 12$ mm as shown in Fig. 7. This maximum signal peak which always corresponds to the highest axial velocity, is believed to be due to the ions from the nearest portion of the acceleration channel for each measurement.

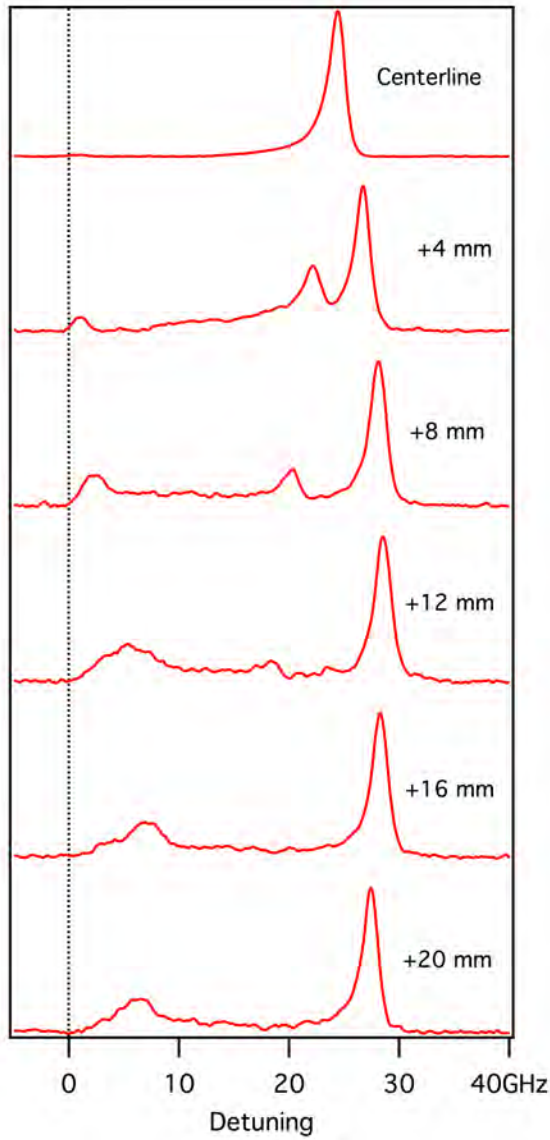


Fig. 8 Evolution of Kr II fluorescence lineshape with distance from centerline. Note that all fluorescence curves are normalized to peak value.

The near zero velocity peak seen in Fig. 8 increases in velocity, and relative magnitude as the measurements move away from the plume centerline. Interestingly, the velocity reaches a maximum near the annular acceleration channel geometric outer edge at $Y = \pm 16$ mm. This low velocity feature is believed to be due to a late ionization population. This is supported by the broad population of ions between the highest energy and the zero velocity that appears to some extent in all the traces. Alternatively, there may be some degree of collisionality in the near-plume that produces this effect.

A third peak appears in Fig. 8 at intermediate velocities between the high and low velocity peaks. At plume centerline, this peak appears to overlap the high velocity peak. As measurements move away from the plume centerline, the peak magnitude and velocity fall.

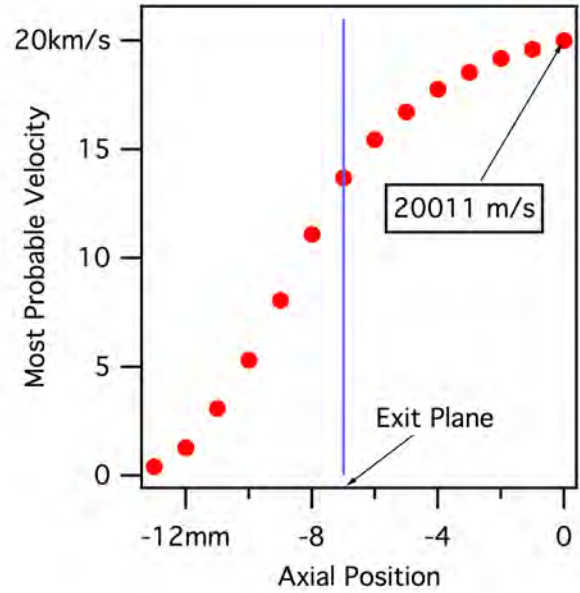


Fig. 9 Most probable velocities as determined from the peak of each fluorescence trace along acceleration channel centerline ($Y = 12$ mm).

By $Y = \pm 16$ mm, this feature is no longer distinguishable in the fluorescence traces. This peak appears to be due to the flux of ions emanating from the opposite side of the acceleration channel annulus from the measurement. This appears consistent with close examination of Fig. 7 in comparison with Fig. 8 from which much of this behavior becomes evident. For example, the $Y = +12$ mm axial velocity of 20.8 km/s can be compared to the axial velocity of this intermediate velocity peak at $Y = -12$ mm, 13.4 km/s. These values match the expected component due to the 40° angle between the measurement axis and the geometrical distance from the exit plane ($\Delta Y = 24$ mm and $\Delta Z = 20$ mm).

Acceleration within Thruster to Near-Plume

Figure 9 shows the most probable velocity measured at the acceleration channel center ($Y = 12$ mm) between the tip of the nose cone ($Z = 0$) and the deepest optical access ($Z = -13$ mm), 6 mm within the thruster. In these data, we see a smooth increase in velocity from near 0 m/s, deep within the thruster, to approximately 20 km/s at $Z = 0$, which denotes the furthest axial extent of the nose cone. From these data, we see that approximately 70% of the acceleration occurs within the physical confines of the thruster. However, significant acceleration also occurs in the near-plume just outside the annular thruster acceleration channel.

Similarly, Fig. 10 shows the variation of Kr II kinetic energy as calculated from the peaks of the fluorescence traces. We deem this to be the *most probable ion kinetic energy*. From these data, we see that the majority of the energy deposition into the ionized

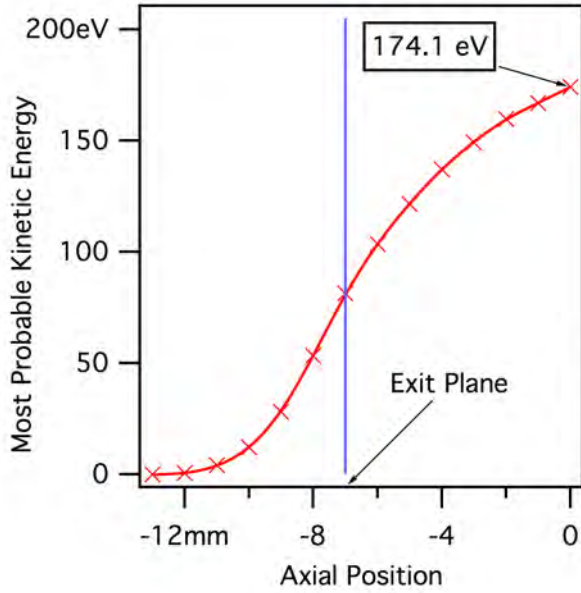


Fig. 10 Most probable kinetic energies as determined from most probable velocities along acceleration channel centerline ($Y = 12$ mm).

propellant is external. The ion energies are only approximately 80 eV at the exit plane and reach approximately 175 eV by the axial extent of the nose cone. Interestingly, the peak ion energy at $Y = \pm 12$ mm at $Z = 13$ mm is approximately 190 eV. Therefore, this limited data set captures the majority of the axial propellant energy deposition.

Using peak, or most probable ion kinetic energies, also allows us to calculate the magnitudes of the effective electric field acting on the ions. As shown on Fig. 10, this calculation is performed by fitting a smoothing spline to these data and then differentiating. This produces an approximation of the effective electric field accelerating the Kr II propellant as shown in Fig. 11. Here, the calculated effective electric field peaks at 28 kV/m approximately 1 mm within the annular acceleration channel. The electric field variation is steepest within the interior and decreases more gradually in the plume, paralleling the radial magnetic field strength, which strongly influences plasma conductivity.

Figure 12 shows the raw fluorescence traces mapped from frequency detuning to velocity space. These data correspond to the velocities in Fig. 9 and span the same spatial range. Please note that the relative ratios of the signals are not directly comparable since these data are scaled to unity area and not scaled between the traces. The value of this presentation is that the raw fluorescence traces approximate the ion velocity distributions. Unity area normalization allows us to illustrate the acceleration of these ions within each sample irrespective of partial occlusion of the collection optics.

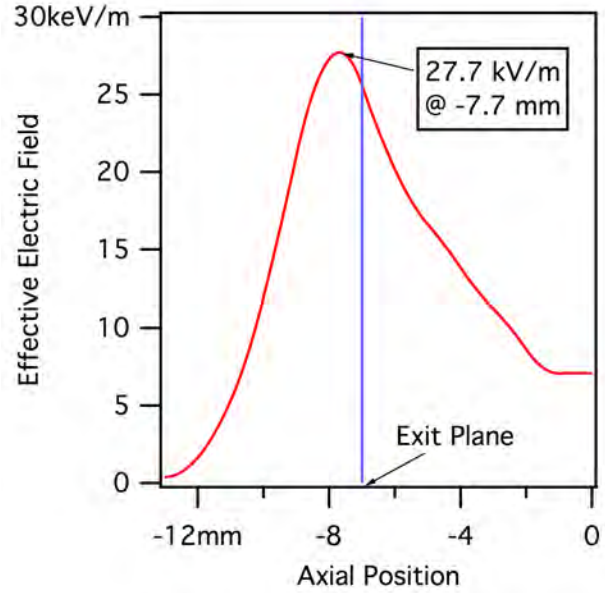


Fig. 11 Effective electric field as calculated from most probable kinetic energies along acceleration channel centerline ($Y = 12$ mm).

Comparison of the various traces in Fig. 12 does provide a qualitative understanding of the ionization and acceleration process in this thruster. At the furthest into the thruster that affords optical access ($Z = -13$ mm), we see a very sharp peak with a small positive velocity. Here, the ionization process is occurring and substantial acceleration of the ions has not yet occurred. The height of this peak drops substantially and the distribution broadens until approximately $Z = -9$ mm. In this region, we hypothesize that the acceleration and ionization regions overlap substantially. This is consistent with the traces in Fig. 12 between $Z = -13$ mm and $Z = -9$ mm where a continuum of stationary to accelerated ions is clearly shown.

Interestingly, $Z = -8$ mm is also the peak of the calculated effective electric field, and at this position, the character of the velocity distributions (as characterized by the fluorescence traces in Fig. 12) changes. At this position and further downstream, the main peak continues to accelerate as shown in Fig. 8, and the peak sharpens slightly, possibly due to small amount of kinematic compression. However, the velocity distributions (as approximated by the raw fluorescence traces) now develop a low level plateau between zero velocity and the main peak. This plateau implies that there is still some ionization occurring. However, it appears that the primary ionization zone has passed, and that only residual ionization is occurring in this region. Obviously, these late stage ions will not recover substantial portions of the applied acceleration potential and will continually lag the primary ion velocity population.

Beyond $Z = -5$ mm (2 mm outside the geometrical channel exit plane), the apparent velocity distributions in Fig. 8 retain a near constant peak with some net acceleration. The low level plateau feature remains constant implying the presence of some external ionization. This is consistent with the $Y = 12$ mm trace in Fig. 8 which shows a continuation of the behavior out to $Z = 13$ mm.

Comparison to previous xenon ion LIF measurements of the same thruster,²² indicate that these krypton distributions are considerably narrower and exhibit improved SNR. This could be due to a number of factors. For one, this data set was taken with a minimized discharge oscillation for thruster operational stability. Previous LIF studies have shown that the magnitude of the breathing mode oscillation is correlated to the width of the velocity distributions. Therefore, reducing discharge channel plasma turbulence will likewise reduce the breadth of the VDF.⁷ Krypton operation also typically displays lower magnitude breathing mode discharge oscillations,²⁴ likely due to differences in the electron mobility, perhaps due to the lower mass, greater mobility of krypton. As a result of most likely a combination of these factors, the krypton LIF traces in this study are typically much sharper and exhibit higher SNR than many previous xenon LIF measurements. Future measurements at conditions optimized for thruster performance may yield results with optimized signals.

Conclusions and Future Work

We have presented the background research of the Kr II $5d^4D_{7/2}-5p^4P_{5/2}^\circ$ transition at 728.98 nm suitable for measuring the flow fields of a highly ionized krypton plasma thruster using LIF. Our measurement survey of the near-plume and acceleration channel ion velocities has demonstrated that this optical transition is suitable for diagnosis of Hall effect thruster plasmas, as well as other rarified krypton plasma thrusters.

Beyond simply repeating LIF measurements already performed on xenon Hall effect thrusters with krypton propellants, there is a lure of increasing fundamental understanding of Hall effect plasma dynamics by studying the differences between krypton and xenon acceleration. For example, the effective electric field in Fig. 11 is nearly identical to that of the nominal case for xenon on the same thruster.²² However, the nominal xenon case has a volumetric flow rate 30% less and a magnetic field approximately 50% greater. Individually, our previous study individually examined xenon cases with 30% higher flow rate, approximately equal to the atomic flux of the krypton case; as well as, the case of a 25% reduction of the applied radial magnetic field. For the xenon measurements, both effects substantially increased the effective magnetic field to approximately 40 kV individually (approximately a 30% increase over the nominal case). Unfortunately,

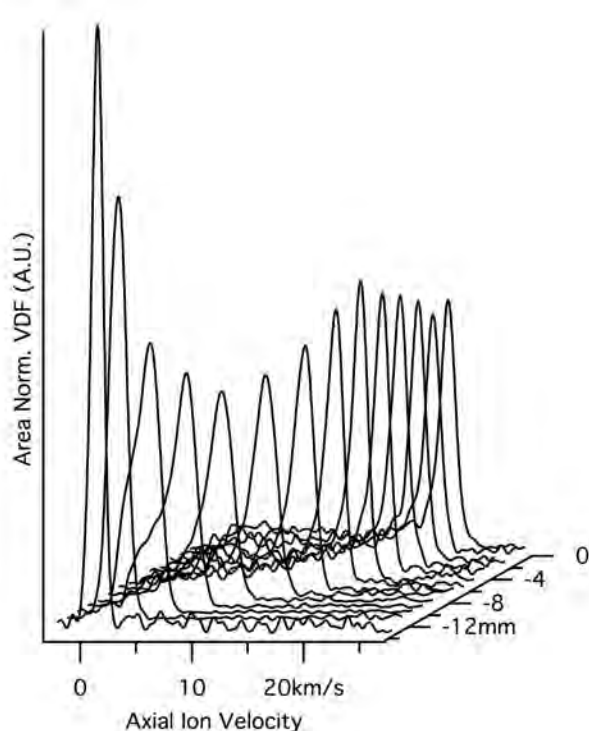


Fig. 12 Scaled fluorescence lineshape illuminating the ionization and acceleration process within the acceleration channel centerline ($Y = +12$ mm) along the Z axis. Note that these data traces are each scaled to unity area and that the exit plane is at $Z = -7$ mm.

the effect of both operating parameter changes has not yet been measured for xenon. Yet, it is interesting that similar operational parameters on xenon raise the effective electric field and that stable operation is only achieved with some difficulty on krypton at a condition that results in an electric field so close to the nominal xenon operating condition. It is obvious that more fundamental comparisons need to be made and that understanding both differences and similarities will lead to better physics based understanding of these devices.

Acknowledgments

The authors are thankful for a number of fruitful discussions that enabled this paper. This includes several early discussions with Dr. M. Cappelli of Stanford University and Dr. D. Scharfe now of AFRL/RZSA. Finally, the paper would not have been written except for the strong encouragement received very early from Dr. C. W. Larson who would have found this paper to be *classically OCD!*

References

- ¹R. Jahn, *Physics of Electric Propulsion*. McGraw-Hill, 1968.
- ²D. R. Lide, *Handbook of Chemistry and Physics*, 79th ed. CRC Press, 1998.

- ³O. Duchemin, D. Valentian, and N. Cornu, "Cryostorage of propellants for electric propulsion," in *Proceedings of the 45th Joint Propulsion Conference and Exhibit*, no. AIAA-2009-4912. American Institute of Aeronautics and Astronautics, August 2009.
- ⁴W. A. Hargus Jr. and M. A. Cappelli, "Laser-induced fluorescence measurements of velocity within a hall discharge," *Applied Physics B*, vol. 72, no. 8, pp. 961–969, June 2001.
- ⁵W. A. Hargus and C. S. Charles, "Near exit plane velocity field of a 200 w hall thruster," *Journal of Propulsion and Power*, vol. 24, no. 1, pp. 127–133, January-February 2008.
- ⁶S. Mazouffre, D. Gawron, V. Kulaev, and N. Sadeghi, "A laser spectroscopic study on xe^+ ion transport phenomena in a 5 kw-class hall effect thruster," in *Proceedings of the 30th International Electric Propulsion Conference*, no. IEPC-2007-160. Florence, Italy: Electric Rocket Society, September 2007.
- ⁷M. R. Nakles and W. A. Hargus Jr., "Background pressure effects on internal and near-field ion velocity distribution of the bht-600 hall thruster," in *Proceedings of the 44th Joint Propulsion Conference and Exhibit*, no. AIAA-2008-5101. Hartford, CT: American Institute of Aeronautics and Astronautics, July 2008.
- ⁸W. A. Hargus Jr., M. R. Nakles, B. Pote, and R. Tedrake, "The effect of thruster oscillations on axial velocity distributions," in *Proceedings of the 44th Joint Propulsion Conference and Exhibit*, no. AIAA-2008-4724. Hartford, CT: American Institute of Aeronautics and Astronautics, July 2008.
- ⁹T. Fujimoto and A. Iwamae, Eds., *Plasma Polarization Spectroscopy*, ser. Series on Atomic, Optical and Plasma Physics. Springer-Verlag, 2008, vol. 44.
- ¹⁰R. Cedolin, "Laser-induced fluorescence diagnostics of xenon plasmas," Ph.D. dissertation, Stanford University, June 1997.
- ¹¹T. Trickl, M. J. J. Vrakking, R. Cromwell, Y. T. Lee, and A. H. Kung, "Ultrahigh-resolution (1+1) photoionization spectroscopy of kr i : Hyperfine structures, isotope shifts, and lifetimes for the $n = 5, 6, 7$ $4p5$ ns rydberg levels," *Physiscal Review A*, vol. 39, no. 6, pp. 2948–2955, 1 March 1989.
- ¹²R. D. Cowan, *The Theory of Atomic Structure and Spectra*. Berkeley, CA: University of California Press, 1981.
- ¹³I. I. Sobelman, *Atomic Spectra and Radiative Transitions*. Berlin: Springer-Verlag, 1992.
- ¹⁴H. E. White, *Introduction to Atomic Spectra*. New York: McGraw-Hill, 1934.
- ¹⁵W. A. Hargus and C. S. Charles, "Near-plume laser-induced fluorescence velocity measurements of a medium power hall thruster," *Journal of Propulsion and Power*, vol. 26, no. 1, pp. 135–141, January-February 2010.
- ¹⁶W. A. Hargus Jr. and M. R. Nakles, "Evolution of the ion velocity distribution in the near field of the bht-200-x3 hall thruster," in *Proceedings of the 42nd Joint Propulsion Conference and Exhibit*, no. AIAA-2006-4991. Sacramento, CA: American Institute of Aeronautics and Astronautics, July 2006.
- ¹⁷D. B. Scharfe, "Alternative hall thruster propellants krypton and bismuth: Simulated performance and characterization," Ph.D. dissertation, Stanford University, Palo Alto, CA, August 2009.
- ¹⁸T. J. Scholl, T. D. Gaily, R. A. Holt, and S. D. Rosner, "Fast-ion-beam laser and laser-rf double resonance measurements of hyperfine structure in 83kr ii ," *Physiscal Review A*, vol. 33, no. 4, pp. 2396–2400, April 1986.
- ¹⁹H. A. Schuessler, A. Alousi, M. Idrees, Y. F. Li, F. Buchinger, R. M. Evans, and C. F. Fischer, "Isotope shifts and hyperfine-structure-splitting constants of the $4d-5p$ transition in kr ii at 729 nm," *Physiscal Review A*, vol. 45, no. 9, pp. 6459–6467, 1 May 1992.
- ²⁰Y. Ralachenko, A. E. Kramida, J. Reader, and . N. A. Team, "Nist atomic spectra data base version 3.1.5," National Institute of Standards and Technology, Gaithersburg, MD, Tech. Rep., July 2010.
- ²¹I. Leybold-Heraeus Vacuum Proucts, *Vacuum Technology its Foundations Formulae and Tables*. Leybold-Heraeus Vacuum Proucts, Inc., 1987.
- ²²W. A. Hargus and M. R. Nakles, "Ion velocity measurements within the acceleration channel of low-power hall thruster," *IEEE Transactions on Plasma Science*, vol. 36, no. 5, pp. 1989–1997, October 2008.
- ²³B. Barbieri, N. Beverini, and A. Sasso, "Optogalvanic spectroscopy," *Review of Modern Physics*, vol. 62, no. 3, pp. 603–644, July 1990.
- ²⁴M. R. Nakles, W. A. Hargus, J. J. Delgado, and R. L. Corey, "A performacne comparison of xenon and krypton propellant on an spt-100 hall thruster," in *Proceedings of the 32nd International Electric Propulsion Conference*, no. 003. Weisbaden, Germany: Electric Rocket Society, September 2011.